



Effects of In substitution in $Y_{1-x}In_xBaCo_3ZnO_{7+\delta}$ ($0 \leq x \leq 0.5$) cathodes for intermediate temperature solid oxide fuel cells



Matthew West, Soa-Jin Sher, Arumugam Manthiram*

McKetta Department of Chemical Engineering, University of Texas at Austin, Austin, TX 78712, USA

HIGHLIGHTS

- Substitution of In for Y in $(Y,In)BaCo_3ZnO_{7+\delta}$ impedes decomposition at 600–800 °C.
- In substitution does not noticeably affect the electrochemical performance.
- All samples have thermal expansion coefficients similar to SOFC electrolytes.
- The performance of $YBaCo_3ZnO_{7+\delta}$ composite cathode is surface-area limited.
- $YBaCo_3ZnO_{7+\delta}$ exhibits cathode performance similar to $Ba_{0.5}Sr_{0.5}Co_{0.8}Fe_{0.2}O_{3-\delta}$.

ARTICLE INFO

Article history:

Received 27 May 2014

Received in revised form

27 July 2014

Accepted 1 August 2014

Available online 8 August 2014

Keywords:

Solid oxide fuel cells

Cathodes

Phase stability

Polarization resistance

ABSTRACT

$Y_{1-x}In_xBaCo_3ZnO_{7+\delta}$ ($0 \leq x \leq 0.5$) oxides have been investigated as cathode materials for solid oxide fuel cells (SOFCs). While $YBaCo_3ZnO_{7+\delta}$ is observed to decompose after 120 h exposure to SOFC operating temperatures (600–700 °C), all the In-substituted compositions following $Y_{0.9}In_{0.1}BaCo_3ZnO_{7+\delta}$ are phase stable in the range of 600–800 °C. The substitution of In in the range of $0 < x \leq 0.5$ shows a negligible impact on the polarization resistances and activation energies of $Y_{1-x}In_xBaCo_3ZnO_{7+\delta} + Gd_{0.2}Ce_{0.8}O_{1.9}$ (GDC) composite cathodes on 8 mol% yttria-stabilized zirconia (8YSZ) electrolytes. The polarization resistances of $YBaCo_3ZnO_{7+\delta}$ (YBC3Z) + GDC cathodes decrease with decreasing electrolyte particle size, suggesting a strong dependence on the three-phase boundary region. Also, YBC3Z + GDC cathodes in symmetric cells on both 8YSZ and GDC electrolytes shows superior performance in the range of 400–600 °C compared to the well-studied $Ba_{0.5}Sr_{0.5}Co_{0.8}Fe_{0.2}O_{3-\delta}$ (BSCF) cathode. With a low thermal expansion coefficient, low intermediate temperature polarization resistances, and good phase stability, the $Y_{0.9}In_{0.1}BaCo_3ZnO_{7+\delta}$ oxide is an attractive cathode candidate for low and intermediate temperature SOFCs.

© 2014 Elsevier B.V. All rights reserved.

1. Introduction

Solid oxide fuel cells (SOFCs) are power generation devices which offer higher efficiencies, operate with inexpensive catalysts, and are compatible with a wide variety of fuels compared to other fuel-cell technologies [1,2]. Even with these advantages, SOFCs are currently limited from wide-spread commercialization in particular due to materials challenges. One of the main areas of investigation in SOFC research is how to reduce the operating temperature from the conventional 800–1000 °C range to the intermediate-temperature (IT) range of 500–800 °C to alleviate strain from thermal expansion mismatches and to allow for less expensive

interconnect materials, like stainless steel, which is unsuitable at high temperatures [1,2]. However, traditional cathode materials in the IT region offer greatly diminished performance, and alternative cathode materials are being intensively investigated to successfully develop an intermediate-temperature solid oxide fuel cell (IT-SOFC) [3–6].

Many cathode materials investigated for IT-SOFC have been plagued by thermal expansion coefficients (TECs) that are significantly larger than those of the other SOFC components [3,6]. This TEC mismatch presents a problem, as it can lead to delamination of the components when elevated to operating temperatures. In many materials (e.g. $LaBaCo_2O_{5+\delta}$), this thermal expansion is primarily caused by the transition of an octahedral-site Co^{3+} ion from low-spin to high-spin state [4]. Recently, a new series of materials based on $RBa(Co,M)_4O_{7+\delta}$ (R = lanthanide ion, M = transition metal) has been investigated as both oxygen storage materials and

* Corresponding author. Tel.: +1 512 471 1791; fax: +1 512 471 7681.

E-mail address: rmanth@mail.utexas.edu (A. Manthiram).

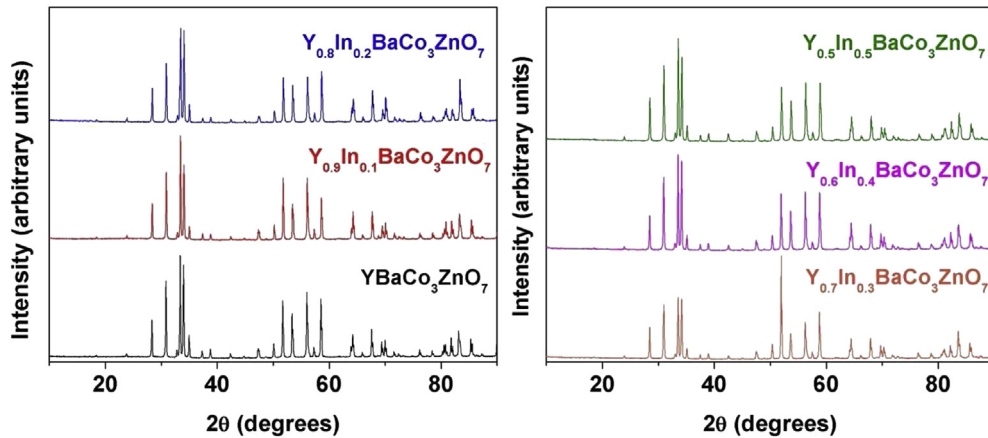


Fig. 1. Room-temperature XRD patterns of the as-synthesized $Y_{1-x}In_xBaCo_3ZnO_{7+\delta}$ ($0 \leq x \leq 0.5$) samples before long-term stability testing.

Table 1

Structural and thermal expansion parameters of $Y_{1-x}In_xBaCo_3ZnO_{7+\delta}$ oxides.

x	a (Å)	c (Å)	Volume (Å ³)	χ^2	R _{Bragg}	TEC 80–900(E ⁻⁶ K ⁻¹)
0	6.32	10.27	353.90	3.48	4.74	9.2
0.1	6.30	10.27	353.29	3.28	6.28	9.4
0.2	6.30	10.26	352.05	6.93	9.38	8.9
0.3	6.29	10.24	350.67	11.6	11.8	9.3
0.4	6.28	10.23	349.50	4.91	5.44	9.2
0.5	6.27	10.22	348.22	3.85	5.04	9.2

by our group as low-TEC cathodes for IT-SOFC [7–11]. These materials do not exhibit any spin-state transition as the cobalt ions are located in tetrahedral sites and therefore always remain in the high-spin configuration with temperature [8].

The $RBa(Co,M)_4O_{7+\delta}$ -based swedenborgite-type materials have limited O^{2-} ionic conductivity, so their electrochemical performance is strongly dependent upon the length of the three-phase boundary region (TPB), or the surface area where the cathode, electrolyte, and oxidant all touch [12]. In order to increase the performance, the $RBa(Co,M)_4O_{7+\delta}$ particles are traditionally mixed with an electrolyte to form a composite cathode to extend the TPB [9,11]. In this form, these materials generally offer satisfactory performance as IT-SOFC cathodes, but unfortunately suffer from inadequate long-term thermal stability at the operating temperatures [7–11].

Previous studies in our group have focused on how substitutions in both the R and M sites of $RBa(Co,M)_4O_{7+\delta}$ affect the long-term thermal stability [7–11]. A substitution of one Zn ion at the M

site greatly improves the stability, but the electrochemical performance suffers as the Zn content increases [8]. A variety of substitutions at the R-site have also been investigated, and each has different effects on stability and performance [7–11]. It was found that an R = Y in $RBaCo_3ZnO_{7+\delta}$ shows good performance and stability at high temperatures ($T \approx 800$ °C), but otherwise decomposes after exposure to the operating temperatures for an extended period [10]. Contrarily, when R = In, the performance and high-temperature stability are generally worse than those with R = Y, but they are stable when held at lower temperatures ($T \approx 600$ °C) [10]. When the two are combined in an equimolar ratio (i.e., R = $Y_{0.5}In_{0.5}$), the material is stable at all temperatures of interest, and the performance falls between that of R = Y and R = In Ref. [10].

In this work, we examine in more detail the effects of In substitution in $Y_{1-x}In_xBaCo_3ZnO_{7+\delta}$ for $0 \leq x \leq 0.5$ between the high-performing R = Y and the fully stabilized R = $Y_{0.5}In_{0.5}$, with the intention of finding the minimum amount of In substitution necessary for stability at all temperatures of interest. The effects of In substitution on crystal chemistry, long-term thermal stability, oxygen content, and electrochemical performance of $Y_{1-x}In_xBaCo_3ZnO_{7+\delta}$ ($0 \leq x \leq 0.5$) are presented.

2. Experimental

The $Y_{1-x}In_xBaCo_3ZnO_{7+\delta}$ samples were synthesized by conventional solid-state reactions (SSR). Required amounts of Y_2O_3 , In_2O_3 , $BaCO_3$, Co_3O_4 , and ZnO were mixed with ethanol in an agate mortar

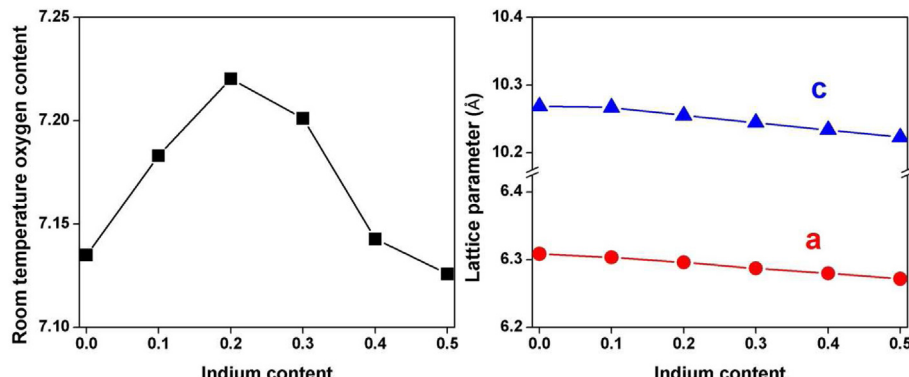


Fig. 2. Room-temperature oxygen contents and lattice parameter values of $Y_{1-x}In_xBaCo_3ZnO_{7+\delta}$ ($0 \leq x \leq 0.5$).

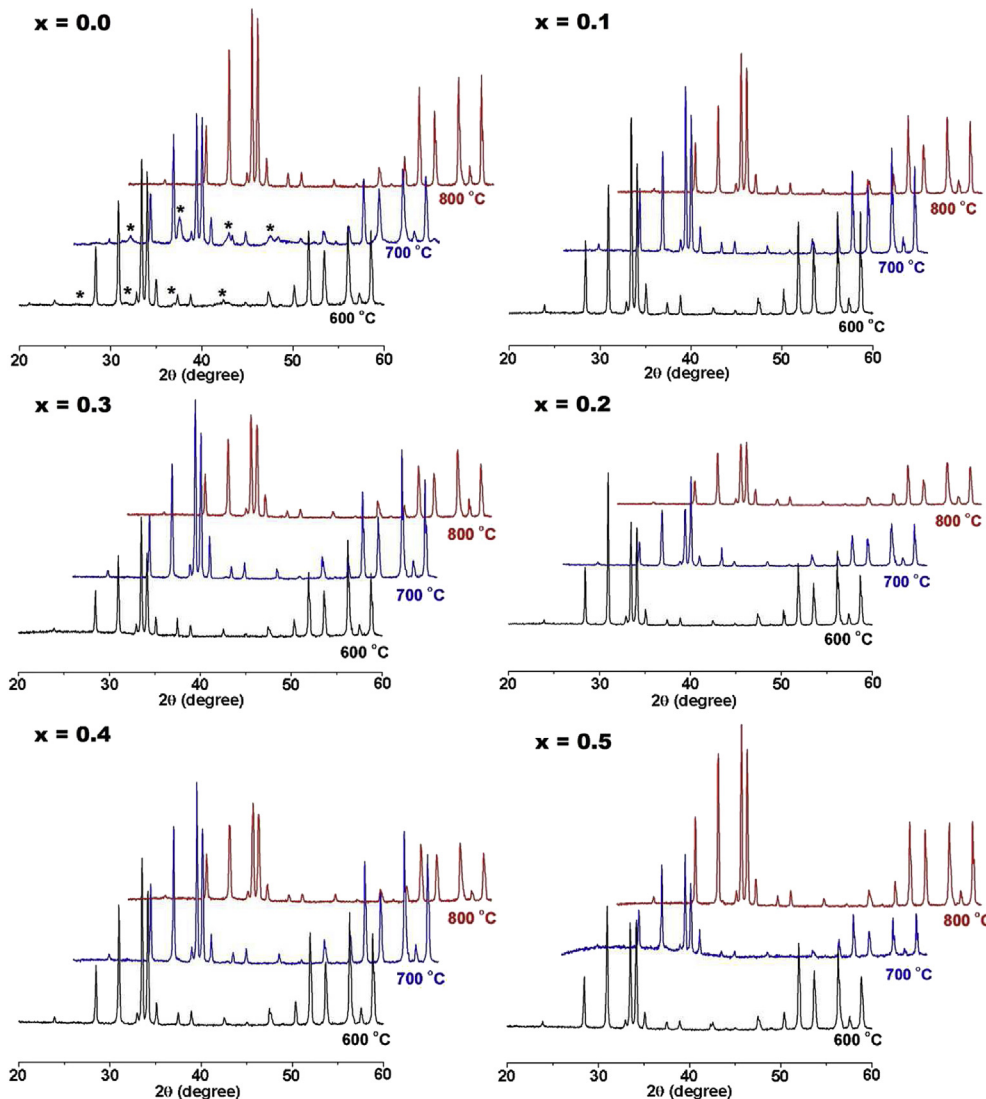


Fig. 3. Room-temperature XRD patterns of the $\text{Y}_{1-x}\text{In}_x\text{BaCo}_3\text{ZnO}_{7+\delta}$ ($0 \leq x \leq 0.5$) samples after 120 h exposure to temperatures of 600, 700, and 800 °C. Peaks marked with * denote $\text{BaCoO}_{3-\delta}$ phase formed due to decomposition.

and pestle for 1 h. The mixtures were dried, pressed into pellets, and calcined at 1000 °C for 12 h [8–11]. The powders were then ground, pressed into pellets, and sintered at 1200 °C for 24 h [8–11]. The resultant powders were annealed in air at 900 °C for 6 h, and slowly cooled to room temperature at a rate of 1 °C min⁻¹. The resultant products were characterized by X-ray diffraction (XRD) with CuK α radiation, and the Rietveld method was employed to refine the data with the aid of the FullProf program [13].

The phase stabilities of the $\text{Y}_{1-x}\text{In}_x\text{BaCo}_3\text{ZnO}_{7+\delta}$ samples were assessed by both a long-term phase stability measurement and a shorter term variable-temperature method [8,11]. For the long-term measurement, the samples were heated in alumina crucibles in a box furnace to a specific high temperature at 2 °C min⁻¹ and were allowed to dwell for 120 h before cooling at the same rate. Three separate tests were conducted, with dwelling temperatures of 600, 700, and 800 °C. The resultant powders were then characterized by XRD [8,11,13]. For the variable-temperature program, the samples were heated at a rate of 5 °C min⁻¹ to 1000 °C where they were allowed to dwell for 4 h, followed by cooling at a rate of 2 °C min⁻¹ with subsequent 4 h dwells every 100 °C in the range of 900–100 °C [8].

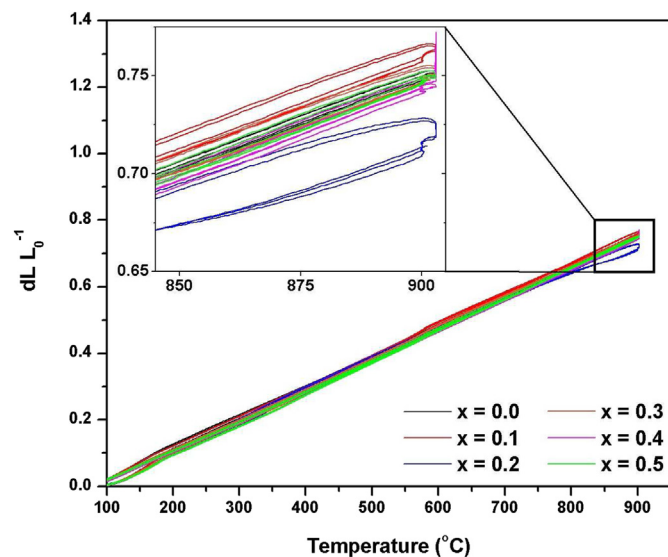


Fig. 4. Thermal expansion behaviors of $\text{Y}_{1-x}\text{In}_x\text{BaCo}_3\text{ZnO}_{7+\delta}$ oxides.

The $\text{Y}_{0.2}\text{Ce}_{0.8}\text{O}_{1.9}$ (YDC) electrolyte was synthesized by the glycine nitrate combustion process (GNP) [14,15]. Required amounts of $\text{Y}(\text{NO}_3)_3 \cdot 6\text{H}_2\text{O}$ and $\text{Ce}(\text{NH}_4)_2(\text{NO}_3)_6$ were dissolved in deionized water (DI) with glycine ($\text{NH}_2\text{CH}_2\text{COOH}$) and heated on a hot plate, forming a viscous gel, until combustion. The resultant powder was then fired at 600°C for 2 h to ensure decarbonation.

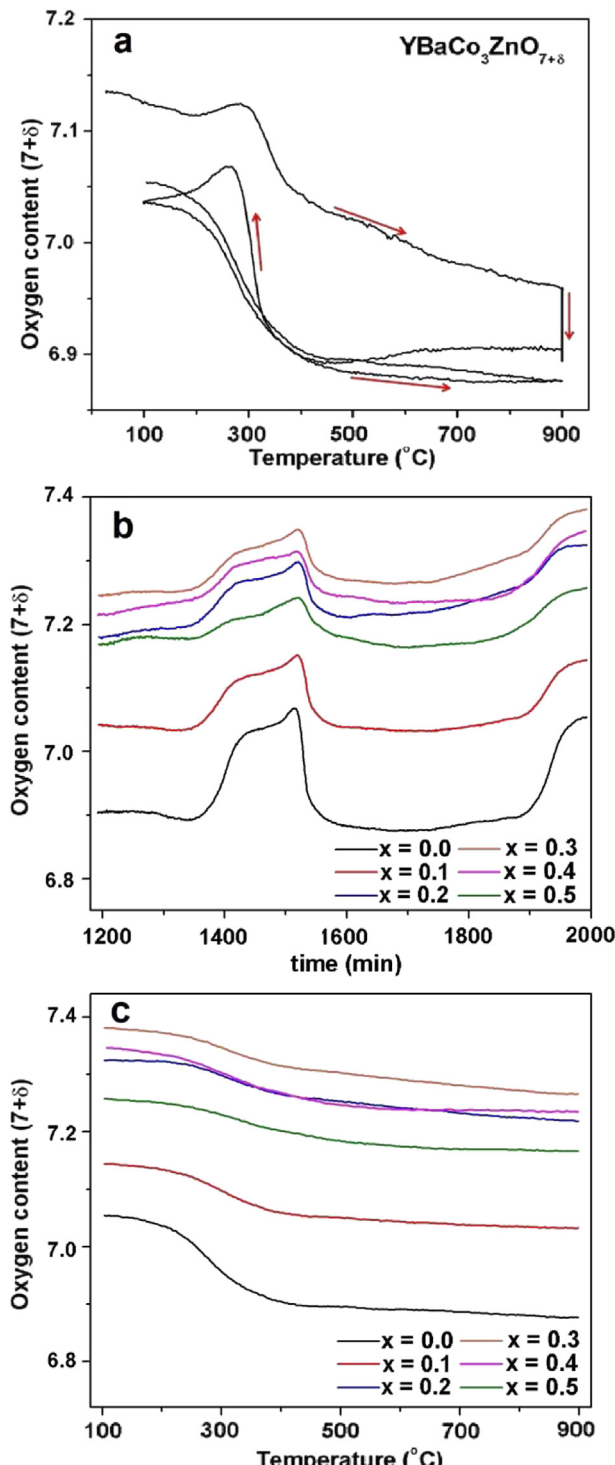


Fig. 5. TGA plots displaying the oxygen content variations of the $\text{Y}_{1-x}\text{In}_x\text{BaCo}_3\text{ZnO}_{7+\delta}$ oxides: (a) full curve of $\text{YBaCo}_3\text{ZnO}_{7+\delta}$ vs. temperature as an example, (b) oxygen content of the samples with time after the 15 h dwell at 900°C , and (c) final cooling curve of the samples.

Composite cathodes were created by ball-milling $\text{Y}_{1-x}\text{In}_x\text{BaCo}_3\text{ZnO}_{7+\delta}$ and $\text{Gd}_{0.2}\text{Ce}_{0.8}\text{O}_{1.9}$ (GDC) powder mixtures in a 50%:50% weight ratio in ethanol for 12–36 h [9–11]. The composite cathode powders were then mixed with an organic binder (Heraeus V006) in a 60%:40% cathode:binder weight ratio to create an ink [9–11]. The GDC powder was synthesized by both solid-state reaction and GNP methods [14,15]. The solid-state method involved ball-milling required amounts of CeO_2 and Gd_2O_3 in ethanol for 12–36 h, with a 1% mol ratio metals basis of $\text{Ni}(\text{NO}_3)_2$ added as a sintering aid [16,17]. This mixture was then dried, pressed into pellets, and sintered at 1550°C for 24 h. The GNP method for GDC is the same as that for YDC, mixing required quantities of $\text{Gd}(\text{NO}_3)_3 \cdot 6\text{H}_2\text{O}$ in place of $\text{Y}(\text{NO}_3)_3 \cdot 6\text{H}_2\text{O}$.

For a comparison, $\text{Ba}_{0.5}\text{Sr}_{0.5}\text{Co}_{0.8}\text{Fe}_{0.2}\text{O}_{3-\delta}$ (BSCF) cathode material was also synthesized by solid-state reaction. Required amounts of BaCO_3 , SrCO_3 , Co_3O_4 , and Fe_3O_4 were mixed by hand in ethanol in an agate mortar and pestle, dried, and calcined at 1000°C for 12 h. The resultant powder was then pressed into pellets, sintered at 1100°C for 20 h, followed by annealing at 900°C for 6 h with a slow 1°C min^{-1} cooling rate to maximize the oxygen content [18]. BSCF and YDC were mixed with an organic binder to create inks as described previously with $(\text{Y},\text{In})\text{BaCo}_3\text{ZnO}_{7+\delta}$ + GDC composite cathode inks.

Thermal expansion data were collected with a dilatometer (Linseis L75H) during three heating and cooling cycles between 80 and 900°C at a rate of 3°C min^{-1} . The sample pellets used during thermal expansion were made by ball-milling the $\text{Y}_{1-x}\text{In}_x\text{BaCo}_3\text{ZnO}_{7+\delta}$ powders for 48 h in ethanol, drying the resultant powder, mixing the said powder with a binder (Butvar B76) in ethanol, drying, pressing, and sintering at 1200°C for 6 h. The oxidation state of cobalt and the oxygen content at room temperature were determined by the iodometric titration [19]. Thermogravimetric analysis (TGA) was conducted with a Netzsch STA 449 F3 thermal analysis system. TGA data were collected during two consecutive heating/cooling cycles at a rate of 3°C min^{-1} from 80 to 900°C , with a 15 h dwell at 900°C after the first heating cycle [8].

The polarization resistances (R_p) of the $\text{Y}_{1-x}\text{In}_x\text{BaCo}_3\text{ZnO}_{7+\delta}$ + GDC composite cathodes were measured on 8 mol% yttria-stabilized zirconia electrolyte supported symmetric cells (8YSZ) in the range of 600 – 800°C by AC impedance spectroscopy (Solartron 1260 FRA). The effective area of all electrodes was 0.25 cm^2 . The electrolyte thickness was between 150 and 200 μm (FuelCellMaterials.com). To prevent interfacial reactions between the composite cathode and the electrolyte, an intermediate layer of

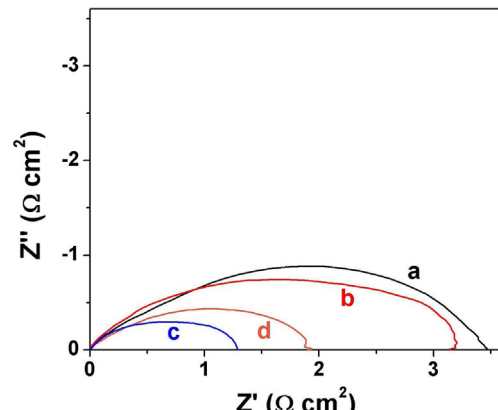


Fig. 6. Area-normalized AC impedance spectra of $\text{YBaCo}_3\text{ZnO}_{7+\delta}$ + GDC symmetric cells with varying current collectors: (a) undiluted silver dots, (b) dilute screen-printed silver paste, (c) screen-printed silver paste with dispersant, and (d) pristine $\text{YBaCo}_3\text{ZnO}_{7+\delta}$.

YDC was screen-printed on both sides and sintered at 1250 °C for 1 h [8,20,21]. The composite cathode layers were then screen-printed three times on each side and sintered for 3 h at 900 °C. Silver paste (FuelCellMaterials), mesh, and wires were used as current collectors. The silver paste was mixed with a small amount of dispersant and screen-printed on both cathodes before attaching the silver mesh and leads. The current collectors were then sintered at 800 °C for 1 h with 1 °C min⁻¹ heating and 2 °C min⁻¹ cooling. The polarization resistances of BSCF were measured on 8YSZ electrolyte supports with the YDC buffer layer as previously described. The BSCF cathode ink was screen-printed three times on each YDC buffer layer and was sintered at 850 °C [22]. Silver current collectors were applied as previously described. After the electrochemical impedance spectroscopy (EIS) measurement, the microstructures of all symmetric cells were examined by a JEOL JSM-5610 scanning electron microscope (SEM). The R_{ps} of the

YBaCo₃ZnO₇ + GDC and BSCF cathodes were also measured on symmetric cells in the range of 400–600 °C with approximately 0.6 mm GDC electrolyte supports synthesized by solid-state reaction and ground to target thickness with a diamond wheel.

To observe the effect of microstructure on symmetric cell impedance, two new cells were manufactured; one cell with YBaCo₃ZnO_{7+δ} + GDC by GNP and another cell with YBaCo₃ZnO_{7+δ} + GDC by GNP that included a small amount of graphite as a pore forming agent. For fabricating the cells, the YBC3Z powder was first ball-milled for 12–36 h in ethanol and then dried. Afterward, this powder was ball-milled for 15 min with an equal mass of GDC synthesized by GNP for the first cell; for the second cell, the powder was ball-milled for 15 min with an equal

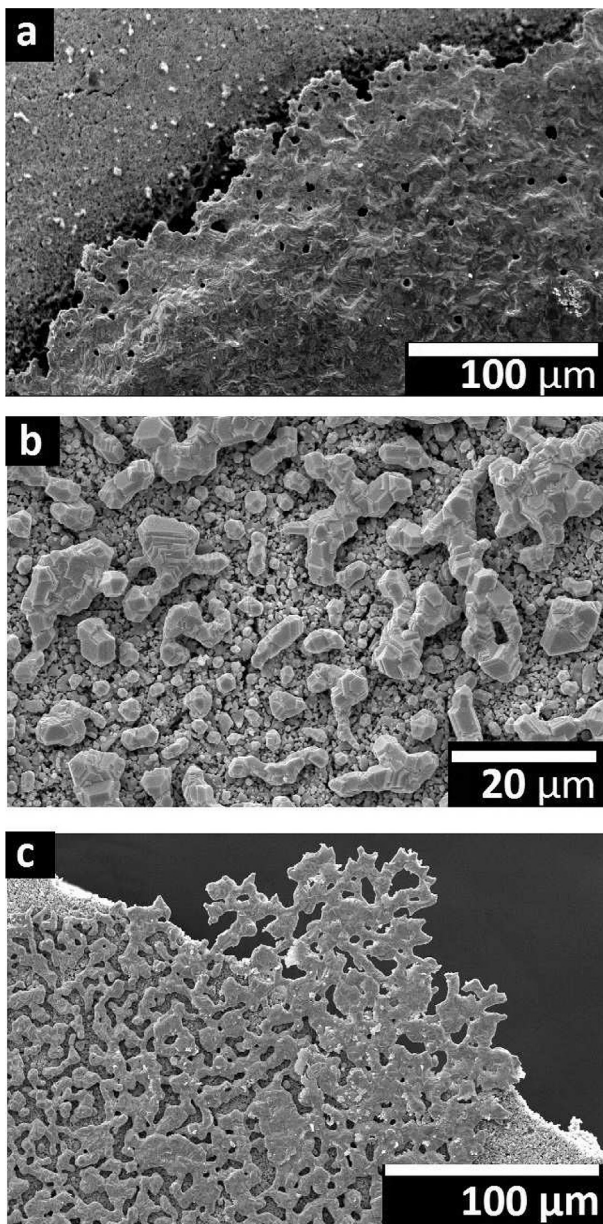


Fig. 7. SEM micrographs of the various silver current collectors: (a) undiluted silver dots, (b) dilute screen-printed silver paste, and (c) screen-printed silver paste with dispersant.

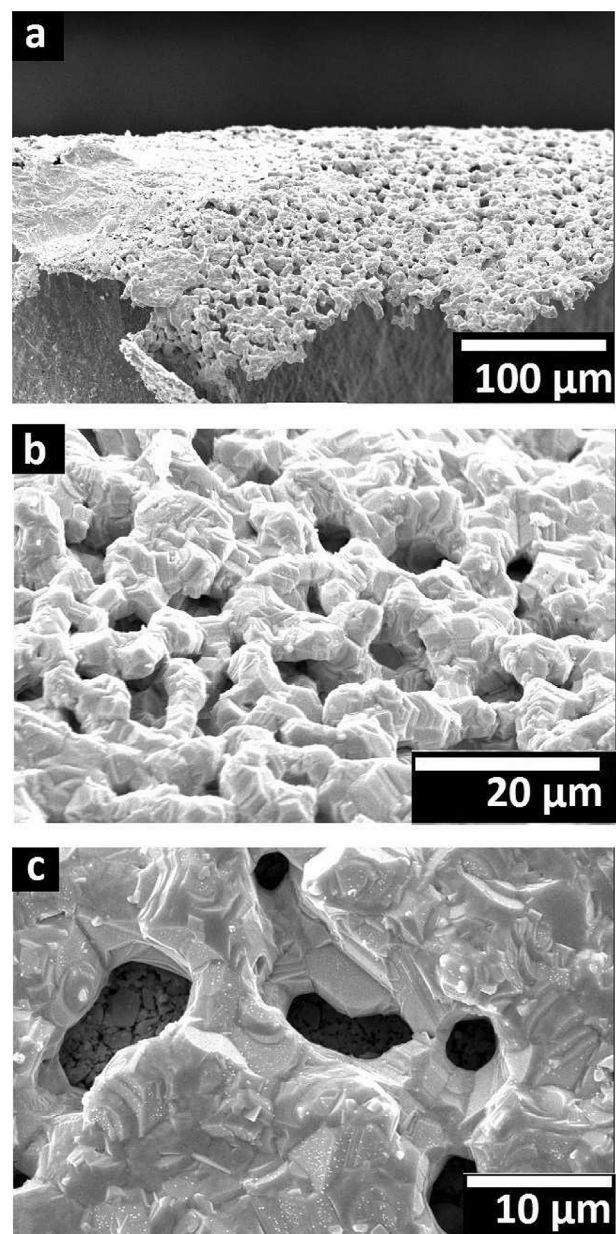


Fig. 8. SEM micrographs displaying the microstructure of the microscale mesh resulting from screen-printing and heat treating the dispersed silver paste. Images (a) and (b) both show the same section of mesh at different magnifications. Image (c) is included to feature the grade of the mesh. These images show the degree of interconnectivity and strength of the current collector, while featuring pore sizes below 10 microns.

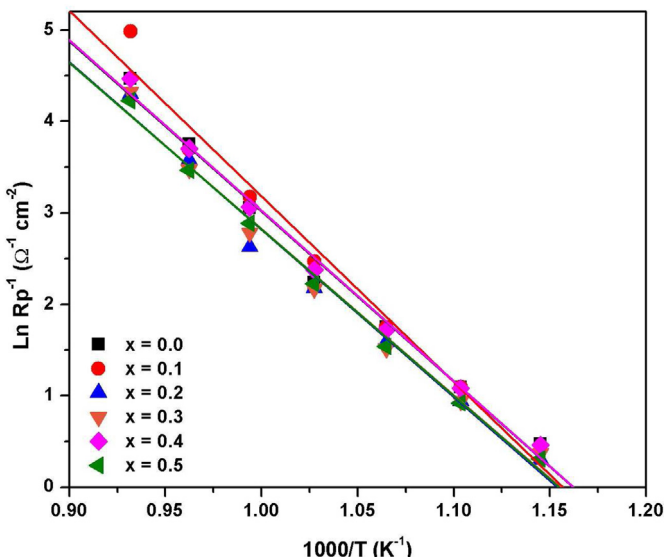


Fig. 9. Arrhenius plots of the $\text{Y}_{1-x}\text{In}_x\text{BaCo}_3\text{ZnO}_{7+\delta}$ + GDC symmetric cells in the range of 600–800 °C.

Table 2
Electrochemical performance data of the $\text{Y}_{1-x}\text{In}_x\text{BaCo}_3\text{ZnO}_{7+\delta}$ + GDC symmetric cells.

X value	E_a 600–800 °C (eV)
0	1.603
0.1	1.565 ^a
0.2	1.577
0.3	1.566
0.4	1.605
0.5	1.570

^a Value shown is as measured from 600 to 766 °C since the value at 800 °C deviated from linearity.

mass of GDC synthesized by GNP along with 5 wt. % graphite as a pore former that was to be removed later by combustion. This powder was then dried and mixed into an ink as previously described. The symmetric cell preparation process was the same as previously described for $\text{Y}_{1-x}\text{In}_x\text{BaCo}_3\text{ZnO}_{7+\delta}$ symmetric cells.

3. Results and discussion

3.1. Crystal chemistry and phase stability of $\text{Y}_{1-x}\text{In}_x\text{BaCo}_3\text{ZnO}_{7+\delta}$ ($0 \leq x \leq 0.5$)

The room-temperature XRD patterns of the $\text{Y}_{1-x}\text{In}_x\text{BaCo}_3\text{ZnO}_{7+\delta}$ ($0 \leq x \leq 0.5$) oxides are shown in Fig. 1. All samples were found to be single-phase oxides with the trigonal P31c space group [10]. Unit cell parameters obtained by refinements and room-temperature oxygen contents obtained by iodometric titration are listed in Table 1 and shown in Fig. 2 as a function of indium content. All lattice parameters decrease with increasing indium content due to the substitution of smaller In^{3+} ion ($r = 0.92 \text{ \AA}$) for the larger Y^{3+} ion ($r = 1.019 \text{ \AA}$) [23].

The oxygen contents of the series increase with indium content for $0 \leq x \leq 0.2$, and then decrease for $0.2 \leq x \leq 0.5$; the values at the endpoints ($x = 0$ and $x = 0.5$) agree well with prior characterizations of this system [10]. This variation can be understood through a combination of unit cell volume and chemistry. Previous work has suggested that the excess oxygen in the lattice is primarily oriented to the CoO_4 tetrahedra [24]. As indium has a significantly larger electronegativity (1.78) compared to yttrium (1.22), the substitution of indium leads to a transfer of electron density from cobalt (electronegativity 1.88) to the R site, thereby allowing more oxygen to orient itself to the cobalt [25]. This may be why $\text{InBaCo}_4\text{O}_{7+\delta}$ has a slightly larger oxygen content than $\text{YBaCo}_4\text{O}_{7+\delta}$ [24]. However, as the lattice volume decreases, there is less interstitial space in the unit cell for the excess oxygen to reside, causing a decrease in excess oxygen [7,10]. The local maximum in oxygen content around $x = 0.2$ suggests that the concentration of excess oxygen is dependent upon both the electronegativity and the unit cell volume; at low indium contents, the electronegativity effect dominates, but at higher indium contents, the loss of interstitial space becomes the primary determining factor for the oxygen content.

The short term phase stabilities of the $\text{Y}_{1-x}\text{In}_x\text{BaCo}_3\text{ZnO}_{7+\delta}$ ($0 \leq x \leq 0.5$) oxides were assessed by a periodic dwelling program in the range of 1000–100 °C as outlined in the experimental section. This program was inspired by the program found by our group previously on similar materials and was utilized to determine if materials would decompose under short-term use [8]. No materials were observed to undergo phase decomposition after being exposed to this program (data not shown here). This correlates well with the prior research on similar compounds, as $\text{YBaCo}_3\text{ZnO}_{7+\delta}$

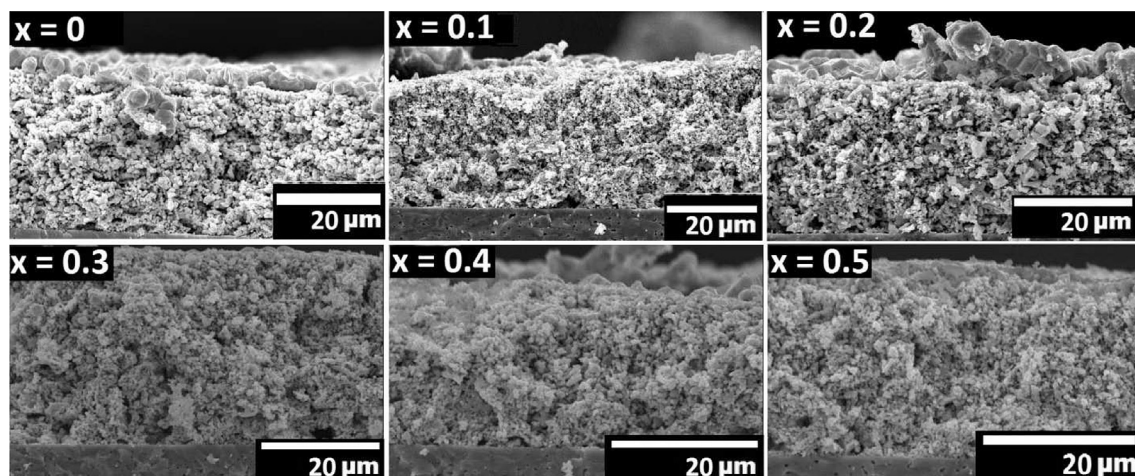


Fig. 10. SEM micrographs of the $\text{Y}_{1-x}\text{In}_x\text{BaCo}_3\text{ZnO}_{7+\delta}$ + GDC symmetric cells (whose performance values can be seen in Fig. 9) after testing.

requires dwelling times above 50 h at elevated temperatures before secondary phases can be observed by XRD [8,10].

The long-term phase stabilities of the $Y_{1-x}In_xBaCo_3ZnO_{7+\delta}$ ($0 \leq x \leq 0.5$) oxides were assessed by heating the single-phase powders to 600, 700, or 800 °C for 120 h, as described in the experimental section. As reported in the previous work, $YBaCo_3ZnO_{7+\delta}$ is stable at 800 °C but partially decomposes at both 600 and 700 °C, while $InBaCo_3ZnO_{7+\delta}$ is stable at 600 °C, but partially decomposes at both 700 and 800 °C [10]. Our group also showed that the sample with a mixture of both ions (i.e., $Y_{0.5}In_{0.5}BaCo_3ZnO_{7+\delta}$) is stable at all temperatures. In this study, as shown in Fig. 3, all samples where $x > 0$ are stable through the entire 600–800 °C region, showing that $x = 0.1$ is all that is required to stabilize the phase. As discussed in our previous work, the instability of the $RBa(Co,M)_4O_{7+\delta}$ series of oxides originates from the presence of tetrahedrally coordinated high-spin $Co^{2+/3+}$ ions [8]. The primary decomposition products of the $RBa(Co,M)_4O_{7+\delta}$ oxides are $BaCoO_{3-z}$ and Co_3O_4 , both of which contain octahedrally coordinated cobalt ions ($Co^{3+/4+}$ and $Co^{2+/3+}$ ions, respectively) [7–11]. Under oxidizing conditions at low temperatures, cobalt tends to exist as low-spin Co^{3+} , which has a large octahedral-site stabilization energy (OSSE), resulting in the above decomposition products [4,8]. Due to the strong preference of Zn^{2+} ions for tetrahedral coordination, the substitution of one Zn^{2+} ion (resulting in $RBaCo_3ZnO_{7+\delta}$) provides stability at shorter times, although depending on the composition of the R-site, long-term stability may not be achieved [8–11]. The stabilization effect of indium observed in this work may be due to both the increased oxygen content and the decreasing lattice volume. Increasing indium content corresponds with decreasing unit cell volume, which is known to increase the decomposition temperature of this class of materials [7]. These results suggest a complex relationship between the composition of the R-site and the overall thermodynamic stability of these materials, and further investigation is required to better understand these phenomena.

3.2. Thermal expansion and oxygen content of $Y_{1-x}In_xBaCo_3ZnO_{7+\delta}$ ($0 \leq x \leq 0.5$)

The thermal expansion behaviors of these materials were assessed with a dilatometer in air in the temperature range of 80–900 °C, and are shown in Fig. 4. These measurements were taken along three sequential heating and cooling curves to account for experimental variance, and the TECs were calculated ignoring the first heating curve. These values are given in Table 1. All TECs fall in the range of $8.9–9.4 \times 10^{-6} K^{-1}$, with no observable trend. As all of these values differ by a very small amount and are in good agreement with previously reported data on similar materials, it is clear that the substitution of indium for yttrium has negligible effect on thermal expansion behavior, and any observed differences are due to experimental variance, e.g. minute microstructural defects in the prepared sample pellets, as previous experiments showed that both YBC3Z and $Y_{0.5}In_{0.5}BaCo_3ZnO_{7+\delta}$ have identical thermal expansion coefficients [10].

The variations of oxygen content with temperature were assessed with TGA in air along two separate heating and cooling cycles with a 15 h dwell at 900 °C during the first heating cycle to allow for oxygen saturation and ensure equilibrium. This data can be seen in Fig. 5. The complete oxygen content trajectory of $YBaCo_3ZnO_{7+\delta}$ is shown in Fig. 5a for reference; in Fig. 5b and c, trajectories for the full series have been truncated for clarity. After equilibrating at high temperatures, all samples are observed to reversibly gain mass as hyperstoichiometric interstitial oxygen upon cooling at approximately 300 °C, as in previous studies [7–11]. Interestingly, for all materials in this series, it is not until

after the third temperature cycle that the oxygen content upon heating and cooling show similarity. In addition, the oxygen contents immediately after the high-temperature annealing increase with indium content for $0 \leq x \leq 0.3$, and decrease for $0.3 \leq x \leq 0.5$, which agrees well with the room-temperature oxygen content trend observed in Fig. 2. Overall, the degree of oxygen content variability during thermal cycling decreases with increasing indium content, which agrees with other work [24]. These plots show that as the electronegativity of the R-site atoms increase, the samples show a tendency to increase affinity for a higher oxygen content, which is eventually overcome by the decreasing lattice volume as the indium substitution increases past 30%.

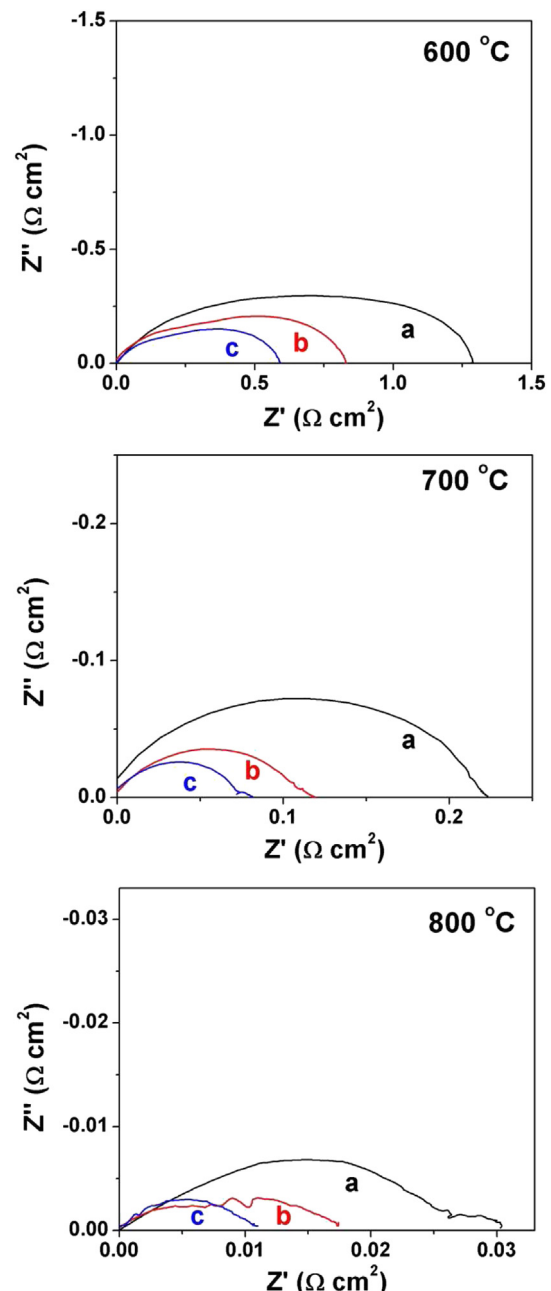


Fig. 11. Nyquist plots providing the effects of the microstructure of the $YBaCo_3ZnO_{7+\delta}$ + GDC symmetric cells on 8YSZ electrolytes, showing the impedance with (a) GDC synthesized by solid-state reaction, (b) GDC synthesized by GNP, and (c) GDC synthesized by GNP with 5 wt. % graphite as pore former. Note that the 800 °C plots use a Bézier curve fitting to reduce signal noise.

3.3. Symmetric cell optimization and electrochemical performances of $Y_{1-x}In_xBaCo_3ZnO_{7+\delta}$ ($0 \leq x \leq 0.5$) + GDC cathodes

Electrochemical performances of the $Y_{1-x}In_xBaCo_3ZnO_{7+\delta}$ + GDC composite cathodes were measured by AC impedance spectroscopy in air with cathode|buffer layer|8YSZ|buffer layer|cathode symmetric cells utilizing 0.2 mm thick electrolytes. The cathodes were prepared by ball-milling equal masses of $Y_{1-x}In_xBaCo_3ZnO_{7+\delta}$ with GDC electrolyte, as previous research has found this to be the optimal ratio for minimizing the polarization resistance (R_p) of the symmetric cells [9]. Since the previous research used micron-grade commercial powder, the GDC electrolyte chosen for these tests was synthesized by solid-state reaction with a small amount of Ni sintering aid to better match the particle size compared to the GNP electrolyte. Buffer layers were included to prevent side-reactions between the cobalt-containing cathode and the zirconia-based electrolyte; YDC was selected for this purpose, as GDC and 8YSZ are known to form a non-conducting interface layer at higher temperatures [20,21]. Silver was chosen as the current collector for its high electrical conductivity, chemical stability, and favorable oxygen reduction kinetics [26–28].

The silver current collector was applied in three different ways: screen printing of silver paste diluted with the Heraeus organic binder; screen printing of the paste diluted with a dispersant; and as small dots of undiluted paste at each corner and the center of the cathode. A fourth sample of screen-printed pristine YBC3Z was used as a reference current collector. The Nyquist plots of symmetric cell impedances at 600 °C of the $YBaCo_3ZnO_{7+\delta}$ + GDC cathode with these variations are presented in Fig. 6, and the SEM images taken after testing are shown in Fig. 7. Of the silver current collectors, the dispersed silver shows the best performance. The undiluted silver dots formed a thick, nonporous silver layer, which impeded the cathode's access to atmospheric oxygen (see Fig. 7a), and the diluted silver paste did not create sufficient electrical conductivity pathways (Fig. 7b). The dispersed silver paste, however, formed a fine micron-scale mesh across the cathode (Fig. 7c). Fig. 8 shows this mesh from multiple angles. This mesh allowed the cathode ample access to oxygen while still uniformly delivering electrons, serving as an exceptional current collector. The pristine YBC3Z did not perform as well as this silver current collector, due primarily to non-ideal sintering and limited electronic conductivity [8].

Fig. 9 shows the Arrhenius plots of the polarization resistances of the $Y_{1-x}In_xBaCo_3ZnO_{7+\delta}$ + GDC composite cathodes in the range of 600–800 °C. All the samples have very similar R_p values, indicating that substitution of indium for yttrium has minimal impact

on the electrochemical performance of this cathode in this temperature range. Any perceived differences among the samples at a given temperature can be primarily attributed to experimental variance. Activation energies derived from these Arrhenius plots are presented in Table 2. All samples show similar activation energies, although previous work showed a slight increase from $YBaCo_3ZnO_{7+\delta}$ to $Y_{0.5}In_{0.5}BaCo_3ZnO_{7+\delta}$ [10]. However, the difference was very small, and is likely to be due to experimental variance in the fabrication and testing of these devices. Fig. 10 shows the cross-sectional SEM images of these cells, where there are no discernible variations between microstructures after testing as a function of In content.

To observe the effect of microstructure on the performance, two additional cells with $YBaCo_3ZnO_{7+\delta}$ + GDC were made to compare to the YBC3Z + GDC cell already tested: one using GDC synthesized by GNP, and one using GDC by GNP mixed with 5 wt. % graphite as a pore former. Both samples were tested on 8YSZ electrolytes with YDC buffer layers. Fig. 11 shows the AC impedance spectroscopy Nyquist plots comparing these three cells at varying temperatures. As the electrolyte in these cells has significant electrical resistivity in this temperature range, the diameter of the impedance loops may be used as an adequate approximation of polarization resistances [29–31]. In these plots, it can be seen that there is a significant reduction in polarization resistance when the solid-state-reaction GDC is replaced with the GDC synthesized by the glycine nitrate process. There is a further reduction in polarization resistance when the graphite is added, particularly in the high-frequency region associated with oxygen reduction reaction. This can be understood to be due to the extension of the three-phase boundary region caused by these modifications.

Finally, the impedances of YBC3Z + GDC (synthesized by solid-state reaction), BSCF, and BSCF + GDC were compared on both 8YSZ + YDC electrolytes and on GDC electrolytes. These data are given in Figs. 12 and 13. In Fig. 12, it can be seen that YBC3Z + GDC shows performance comparable to both pristine and composite BSCF on 8YSZ electrolyte throughout the entire temperature range of 400–800 °C. The Arrhenius plots were generated by fitting the raw data with the equivalent circuit shown in Fig. 12b [11]. Fig. 13 shows that YBC3Z + GDC on GDC electrolyte has reduced polarization resistance at lower temperatures ($400^{\circ}\text{C} \leq T \leq 600^{\circ}\text{C}$), but BSCF begins to show improved performance as temperature increases. The composite BSCF shows increased polarization resistance across all temperatures due to its mixed ionic and electronic conducting properties; as BSCF can transport oxide ions on its own, the expansion of the three-phase boundary has less of an effect on performance. This is also supported by the change in the shape of

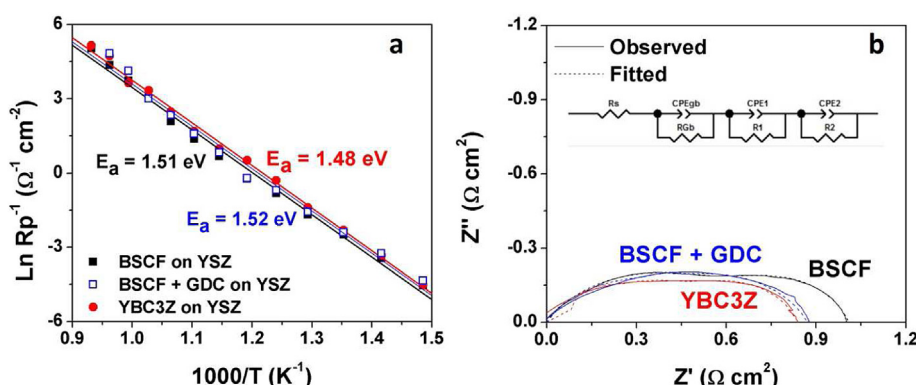


Fig. 12. (a) Arrhenius plots of $YBaCo_3ZnO_{7+\delta}$ + GDC (made by solid-state reaction and labeled here as YBC3Z), BSCF, and BSCF + GDC symmetric cells on 8YSZ electrolytes in the range of 400–800 °C. (b) Nyquist plots of all three cells at 600 °C with the equivalent circuit used to generate the fitted data.

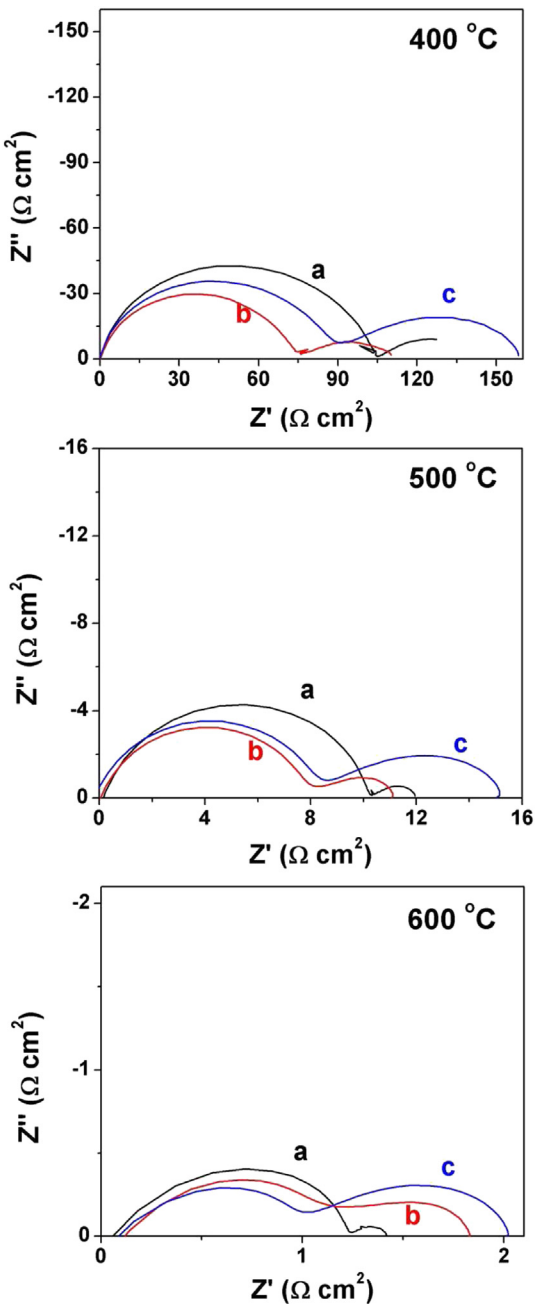


Fig. 13. Nyquist plots comparing (a) BSCF, (b) $\text{YBaCo}_3\text{ZnO}_{7+\delta}$ + GDC, and (c) BSCF + GDC symmetric cells on GDC electrolyte in the range of 400–600 °C.

the Nyquist plot; according to Adler et al. [31,32], the impedance at lower frequencies is attributed to the charge transfer across the electrode/electrolyte boundary, while the impedance at high frequencies is attributed to the catalytic adsorption/reduction of oxygen at the cathode. The inclusion of GDC into the BSCF composite can be seen to slightly reduce the high-frequency impedance due to the increased interface between cathode and electrolyte. Contrarily, the low-frequency impedance section is expanded, due to the reduction in catalytically active oxide surface area. These results show that the performance of the $\text{Y}_{1-x}\text{In}_x\text{BaCo}_3\text{ZnO}_{7+\delta}$ + GDC cathodes rivals that of the well-studied BSCF, and that the performance can be improved through further optimization of the microstructure and manufacturing process. Future work will

investigate these modifications, as well as their effect on microstructural stability and single-cell power densities.

4. Conclusions

The effects of indium substitution in the $\text{Y}_{1-x}\text{In}_x\text{BaCo}_3\text{ZnO}_{7+\delta}$ ($0 \leq x \leq 0.5$) system have been investigated. In contrast to the $x = 0$ sample, all samples with $0.1 \leq x \leq 0.5$ are stable in the 600–800 °C range after 120 h exposures, indicating that a mere $x = 0.1$ indium substitution is capable of stabilizing the lattice and phase. Room-temperature oxygen content values reach a weak maximum around $x = 0.2$, but overall do not vary much with indium content. The oxygen contents of the materials show a similar trend after high-temperature annealing in a TGA in air atmosphere, and the substitution of indium for yttrium inhibits the adsorption/desorption of oxygen during thermal cycling. The thermal expansion properties of the samples do not differ significantly with the substitution of indium, and all the samples show good match with the TECs of the traditional SOFC electrolyte materials. Electrochemical performances are not significantly affected by the substitution of indium in this range, which correlates well to previous findings. Preliminary findings show that the polarization resistance of the cathode can be greatly influenced by the microstructure, as the performance of this class of cathodes is strongly dependent on the three-phase boundary region. $\text{YBaCo}_3\text{ZnO}_{7+\delta}$ + GDC shows a lower polarization resistance than BSCF at temperatures below 600 °C, although BSCF begins to outperform $\text{YBaCo}_3\text{ZnO}_{7+\delta}$ + GDC as temperatures increase 600 °C, revealing that the $\text{Y}_{1-x}\text{In}_x\text{BaCo}_3\text{ZnO}_{7+\delta}$ class of cathodes is particularly attractive for operation below 600 °C.

Acknowledgments

Financial support by the Welch Foundation grant F-1254 is gratefully acknowledged. S.-J. S. was supported by the Research Experience for Undergraduates (REU) program of the National Science Foundation Materials Interdisciplinary Research Team (MIRT) grant DMR-1122603. The authors thank Daeil Yoon and Christina Ortiz for their assistance with some experiments.

References

- [1] D.J.L. Brett, A. Atkinson, N.P. Brandon, S.J. Skinner, Chem. Soc. Rev. 37 (2008) 1568–1578.
- [2] O. Yamamoto, Electrochim. Acta 45 (2000) 2423–2435.
- [3] J.H. Kim, A. Manthiram, J. Electrochem. Soc. 155 (2008) B385–B390.
- [4] J.H. Kim, F. Prado, A. Manthiram, J. Electrochem. Soc. 155 (2008) B1023–B1028.
- [5] J. Kim, A. Jun, J. Shin, G. Kim, J. Am. Ceram. Soc. (2013), <http://dx.doi.org/10.1111/jace.12692>.
- [6] M. West, A. Manthiram, Int. J. Hydrogen Energy 38 (2013) 3364–3372.
- [7] O. Parkkima, H. Yamauchi, M. Karppinen, Chem. Mater. (2013), <http://dx.doi.org/10.1021/cm3038729>.
- [8] J.H. Kim, A. Manthiram, Chem. Mater. 22 (2010) 822–831.
- [9] J.H. Kim, Y.N. Kim, S.M. Cho, H. Wang, A. Manthiram, Electrochim. Acta 55 (2010) 5312–5317.
- [10] Y.N. Kim, J.H. Kim, M.P. Paranthaman, A. Manthiram, J. Power Sources 214 (2012) 7–14.
- [11] Y.N. Kim, J.H. Kim, A. Manthiram, Int. J. Hydrogen Energy 36 (2011) 15295–15303.
- [12] R. O’Hayre, D.M. Barnett, F.B. Prinz, J. Electrochem. Soc. 152 (2005) A439–A444.
- [13] J. Rodríguez-Carvajal, Phys. B 192 (1993) 55–69.
- [14] H. Taguchi, D. Matsuda, M. Nagao, K. Tanihata, M. Yoshinari, J. Am. Ceram. Soc. 75 (1992) 201–202.
- [15] L.A. Chick, L.R. Pederson, G.D. Maupin, J.L. Bates, L.E. Thomas, G.J. Exarhos, Mater. Lett. 10 (1990) 6–12.
- [16] C. Kleinlogel, I.J. Gauckler, Adv. Mater. 13 (2001) 1081–1085.
- [17] J.D. Nicholas, L.C. De Jonghe, Solid State Ionics 178 (2007) 1187–1194.
- [18] S. Li, X. Xie, J. Electrochem. Soc. 160 (2013) F224–F233.
- [19] A. Manthiram, J.S. Swinnea, Z.T. Sui, H. Steinfink, J.B. Goodenough, J. Am. Chem. Soc. 109 (1987) 6667–6669.

- [20] Z. Duan, M. Yang, A. Yan, Z. Hou, Y. Dong, Y. Chong, M. Cheng, W. Yang, *J. Power Sources* 160 (2006) 57–64.
- [21] A. Tsoga, A. Gupta, A. Naoumidis, P. Nikilopoulos, *Acta Mater.* 48 (2000) 4709–4714.
- [22] D. Yoon, Q. Su, H. Wang, A. Manthiram, *Phys. Chem. Chem. Phys.* 15 (2013) 14966–14972.
- [23] R.D. Shannon, *Acta Crystallogr. A* 32 (1976) 751–757.
- [24] H. Hao, J. Cui, C. Chen, L. Pan, J. Hu, X. Hu, *Solid State Ionics* 177 (2006) 631–637.
- [25] W.M. Haynes, T.J. Bruno, D.R. Lide, CRC Handbook of Chemistry and Physics, 94th ed, 2014. <http://www.hbcpnetbase.com/> (accessed 20.02.14).
- [26] H. Huang, T.P. Holme, F.B. Prinz, *ECS Trans.* 3 (2007) 31–40.
- [27] J.H. Shim, Y.B. Kim, J.S. Park, F.B. Prinz, *ECS Trans.* 35 (2011) 2209–2212.
- [28] Y. Guo, Y. Zhou, D. Chen, H. Shi, R. Ran, Z. Shao, *J. Power Sources* 196 (2011) 5511–5519.
- [29] S. Choi, S. Yoo, J. Kim, S. Park, A. Jun, S. Sengodan, J. Kim, J. Shin, H.Y. Jeong, Y.M. Choi, G. Kim, M. Liu, *Sci. Rep.* 3 (2014) 2426.
- [30] M. Liu, H. Hu, *J. Electrochem. Soc.* 143 (1996) L109–L112.
- [31] S.B. Adler, X.Y. Chen, J.R. Wilson, *J. Catal.* 254 (2007) 91–109.
- [32] S.B. Adler, *Chem. Rev.* 104 (2004) 4791–4843.